

# Detection of Television Frequency Interference with Satellite Microwave Imager Observations over Oceans

XIAOLEI ZOU AND XIAOXU TIAN

*Department of Earth, Ocean and Atmospheric Science, Florida State University, Tallahassee, Florida*

FUZHONG WENG

*NOAA/NESDIS/Center for Satellite Applications and Research, College Park, Maryland*

(Manuscript received 21 April 2014, in final form 13 August 2014)

## ABSTRACT

The geostationary satellite television (TV) signals that are broadcasted over various continents can be reflected back to space when they reach ocean surfaces. If the reflected signals are intercepted by the antenna of the microwave imager on board polar-orbiting satellites, they are mixed with the thermal emission from the earth and result in direct contamination of the satellite microwave imager measurements. This contamination is referred to as television frequency interference (TFI) and can result in erroneous retrievals of oceanic environmental parameters (e.g., sea surface temperature and sea surface wind speed) from microwave imager measurements. In this study, a principal component analysis (PCA)-based method is applied for detecting the TFI signals over oceans from the Advanced Microwave Scanning Radiometer for the Earth Observing System (AMSR-E) *Aqua* satellite. It is found that the third principal component of the data matrix of the AMSR-E spectral difference indices from each AMSR-E swath captures the TFI contamination. The TFI-contaminated data on the AMSR-E descending node at both 10.65- and 18.7-GHz frequencies can be separated from uncontaminated data over oceanic areas near the coasts of Europe and the United States based on the intensity of the data projection onto the third principal component (PC). Compared to the earlier methods, the proposed PCA-based algorithm works well on the observations without a priori information and is thus applicable for broader user applications.

## 1. Introduction

The Advanced Microwave Scanning Radiometer (AMSR-E) is a conically scanning microwave imager on board the Earth Observing System (EOS) *Aqua* satellite. It was successfully launched into a polar orbit on 4 May 2002 with an equator-crossing time (ECT) at 1330 (Kawanishi et al. 2003). The six low AMSR-E channels have frequencies at 6.925 (C band), 10.65 (X band), and 18.7 GHz (K band) with both horizontal and vertical polarization, and they are mainly used for retrieving the environmental parameters over oceans (Wilheit et al. 2003) and land (Njoku and Li 1999; Njoku et al. 2003; Kelly et al. 2003). However, these low microwave frequencies operate in unprotected frequency bands. It was found that the C- and X-band AMSR-E measurements

from the earth's natural thermal emission over land can be interfered by the signals from lower-frequency active microwave transmitters, including radar, air traffic control, cell phones, garage door remote controls, GPS signals on highway, defense tracking, vehicle speed detection for law enforcement, etc. (Zou et al. 2012; Zhao et al. 2013). Also, the X- and K-band AMSR-E measurements of the natural thermal emission over ocean could be interfered by the geostationary satellite television (TV) signals reflected off the ocean surfaces. The study investigates the television frequency interference (TFI) detection from satellite microwave imager measurements over oceans. The AMSR-E data are used for testing a new TFI detection technique proposed in this study.

At microwave frequencies, the ocean surface has a large reflectance due to a high permittivity of seawater. The microwave TV signals at the X and K bands broadcasted from geostationary satellites (e.g., Astra, Hot Bird, Atlantic Bird 4A, DirecTV-10/11, etc.) can be reflected off the ocean surfaces. Therefore, satellite-measured passive microwave thermal emission is mixed with the TV signals

---

*Corresponding author address:* Xiaolei Zou, Department of Earth, Ocean and Atmospheric Science, Florida State University, P.O. Box 3064520, Tallahassee, FL 32306-4520.  
E-mail: xzou@fsu.edu

reflected off the ocean. A schematic illustration of an oceanic TFI is provided in Fig. 1. With the expanding demand for fixed-satellite service (FSS) technology, increasing amounts of TFI are now affecting the oceanic measurements from satellite passive microwave instruments (Adams et al. 2010; Truesdale 2013). These TFI-contaminated brightness temperature measurements, if not identified and excluded from the retrieval algorithms, would introduce appreciable errors in the AMSR-E products, such as precipitable water (PW), sea surface wind (SSW), sea surface temperature (SST), and cloud liquid water (CLW) variables (Wentz and Meissner 2000). It is therefore important to develop an effective algorithm to detect TFI-contaminated data prior to carrying out AMSR-E product retrieval and data assimilation over ocean.

TFI detection over oceans is probably more challenging than that over land. The cloud and precipitation can increase the thermal emission and therefore significantly increase the brightness temperature at lower frequencies. Such an increase in AMSR-E-measured brightness temperatures could be of similar magnitude to an increase in brightness temperatures introduced by TFI. Over land, the surface emission is much stronger than that from clouds and precipitation. The C-band and X-band frequency interference can be more detectable without being much affected by the clouds. It is important to develop a robust technique for detecting the oceanic TFI signals while minimizing the “false” TFI signals associated with cloud and precipitation signals.

There are two methods that were employed for identifying TFI signatures over oceans: a chi-square probability method and a regression method (Li et al. 2006). In the chi-square probability algorithm, a TFI detection method is developed using a time-averaged statistical quantity of the retrieval products based on the fact that the source of the oceanic TV signals are fixed in location and time, while the weather signals associated with clouds and precipitation are transient. The goodness of fit (i.e., chi-square probability) is used for TFI detection. The lower the goodness of fit is, the higher the probability of the presence of TFI is expected. In Li et al. (2006), a regression model is first established to predict TFI-free and clear-sky brightness temperatures at X and K bands from the other WindSat channels. Differences between WindSat oceanic observations and the regression-model-predicted brightness temperatures are then used for oceanic TFI detection. The larger the difference, the stronger the TFI intensity is likely to be. The chi-square method looks for geophysical locations where TFI occurs. The regression technique requires TFI-free and clear-sky data for detection.

In this study, a TFI detection algorithm is developed and applied at the pixel level. It is computationally

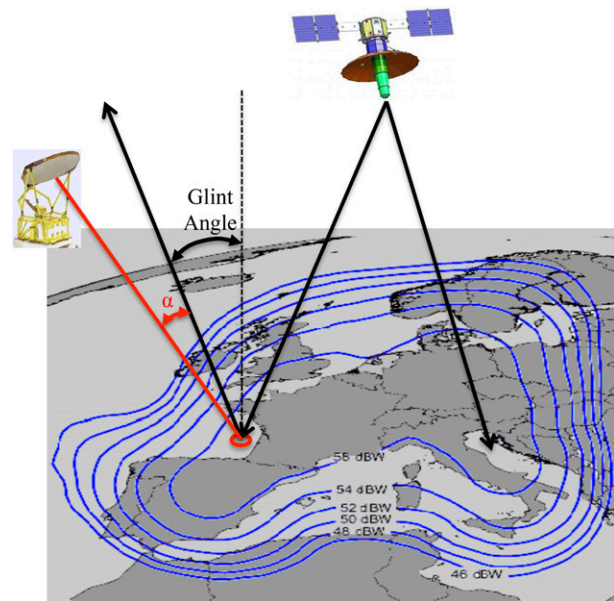


FIG. 1. Schematic illustration of TFI of AMSR-E Earth views (red) with TV signals reflected off ocean surfaces (black dashed). Satellite downlink beam coverage is shown in blue curves, which are obtained from online (<http://www.satsig.net/tooway/tooway-ka-band-downlink-hotbird.gif>). Numbers on the contours indicate the strength of the TV signal expressed in decibel watt. Glint angle is defined as the angle between the reflected ray vector and the normal vector. Variable  $\alpha$  is defined as the angle between the satellite viewing vector and the reflected ray.

efficient. The merits of the algorithm are as follows: (i) it only uses the satellite observations and (ii) it can be applied at the granule or orbit data level. There is no need for training data, a priori determination of rain-free and TFI-free data, and satellite retrieval products. The paper is organized as follows: A brief description of AMSR-E data characteristics is provided in section 2. A new oceanic TFI detection algorithm is carefully described in section 3. Numerical results illustrating the performance of the proposed TFI detection algorithm are presented in section 4. Summary and conclusions are found in section 5.

## 2. AMSR-E data description

AMSR-E is one of the six instruments on board the National Aeronautics and Space Administration (NASA)'s *Aqua* satellite. The *Aqua* satellite was launched into a sun-synchronous orbit at an altitude of 705 km with a swath width of 1445 km (Kawanishi et al. 2003). The ECT of its ascending node is 1330. AMSR-E is a 12-channel, six-frequency, and total power passive microwave imager. Its antenna scans the earth at a constant incidence angle of  $55^\circ$ , and its receiver measures both vertically and horizontally polarized brightness temperatures at 6.925,

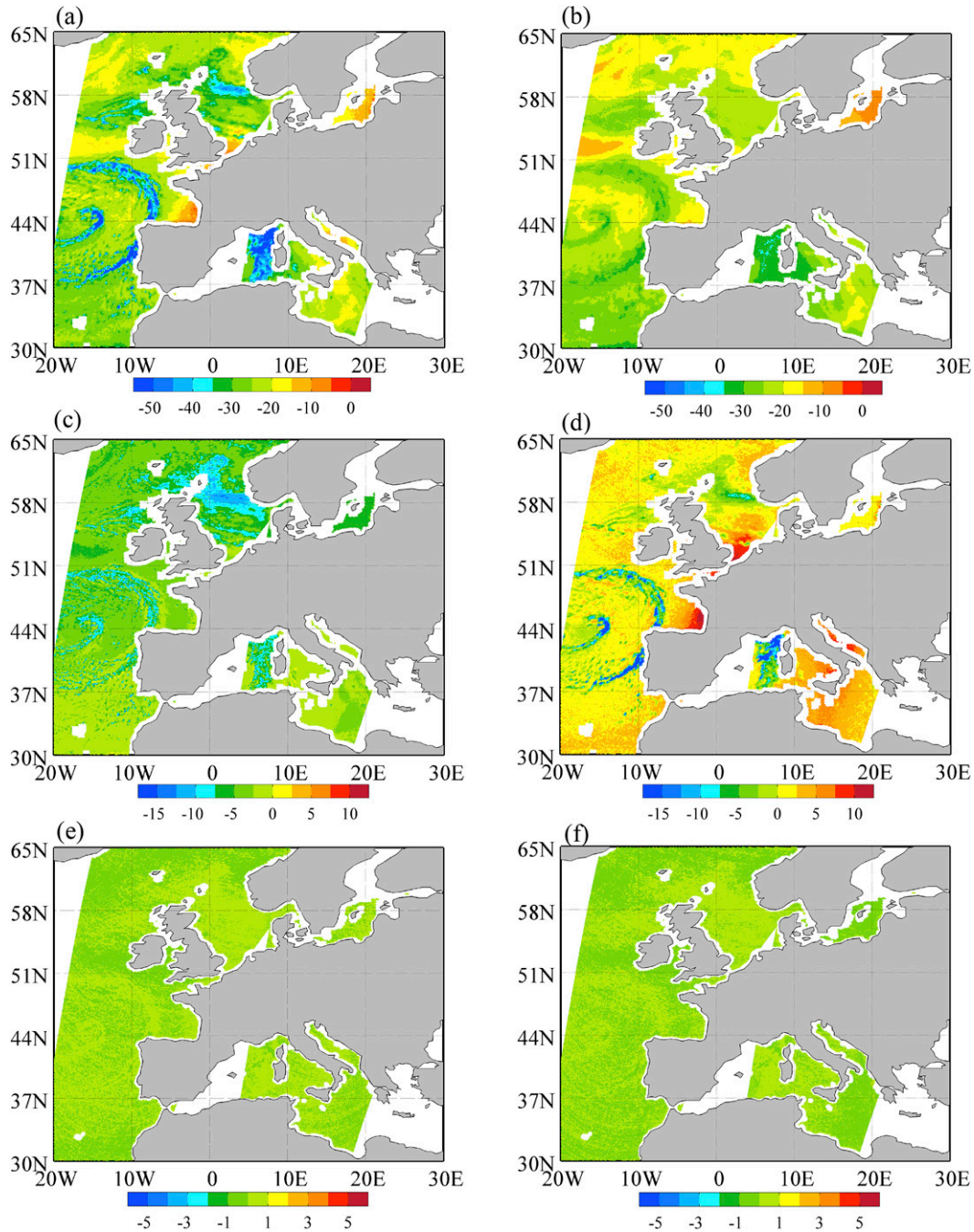


FIG. 2. (a) Spectral differences between  $T_{b,10h}^o$  and  $T_{b,18h}^o$ , as well as (b)  $T_{b,10h}^{A1} - T_{b,18h}^{A1}$ , (c)  $T_{b,10h}^{A2} - T_{b,18h}^{A2}$ , (d)  $T_{b,10h}^{A3} - T_{b,18h}^{A3}$  (TFI signal intensity), (e)  $T_{b,10h}^{A4} - T_{b,18h}^{A4}$ , and (f)  $T_{b,10h}^{A5} - T_{b,18h}^{A5}$  found by the NPCA method on 16 Feb 2011.

10.65, 18.7, 23.8, 36.5, and 89.0 GHz. The across-track and along-track spatial resolutions of the individual ground instantaneous field-of-view (IFOV) measurements increase with frequency. They are 75 km × 43 km at 6.925 GHz, 51 km × 29 km at 10.65 GHz, 27 km × 16 km at 18.7 GHz, 32 km × 18 km at 23.8 GHz, 14 km × 8 km at 36.5 GHz, and 6 km × 4 km at 89.0 GHz. The

sampling interval is 5 km for the highest-frequency channel (89.0 GHz) and 10 km for all other channels.

AMSR-E inherited the Scanning Multichannel Microwave Radiometer (SMMR) on board the *Nimbus-7* and *Seasat* satellites and had some channels in common with the Special Sensor Microwave Imager (SSM/I) on board the Defense Meteorological Satellite Program

(DMSP) and AMSR on board the second *Advanced Earth Observing Satellite (ADEOS II)*. It is worth mentioning that the successor of AMSR-E is AMSR2, which is on board the *Global Change Observation Mission 1st—Water (GCOM-W1)* satellite, which was launched on 18 May 2012. The mission of AMSR2 is similar to that of AMSR-E with two additional channels at 7.3 GHz, which is used for improving the detection and elimination of frequency interferences at 6.925 GHz over land.

### 3. A normalized PCA (NPCA) method for TFI detection

A new oceanic TFI detection algorithm is describe in this section. First, brightness temperatures are normalized to form a vector including all the AMSR-E channels,

$$\mathbf{v}_i = \begin{pmatrix} \frac{T_{b,6h}^o - \mu}{\sigma} \\ \frac{T_{b,6v}^o - \mu}{\sigma} \\ \vdots \\ \frac{T_{b,89h}^o - \mu}{\sigma} \\ \frac{T_{b,89v}^o - \mu}{\sigma} \end{pmatrix}_i = \begin{pmatrix} T_{b,6h}^{(n)} \\ T_{b,6v}^{(n)} \\ \vdots \\ T_{b,89h}^{(n)} \\ T_{b,89v}^{(n)} \end{pmatrix}_i, \quad (1)$$

where  $i = 1, 2, \dots, N$  and  $N$  is the total number of data points over a half orbit (about 2000 AMSR-E scan lines) excluding data over land and sea ice;  $\mu_i$  and  $\sigma_i$  are the mean and standard deviations of brightness temperatures at all frequencies of the  $i$ th data point, respectively. The level 1B (L1B) brightness temperature datasets are used in this study. Since the number of pixels across an AMSR-E scan line at 89 GHz is more than twice the pixels for the other AMSR-E channels, every other pixel of the 89.0-GHz B scans was included in this study to match the pixels of the lower-frequency channels.

The normalized brightness temperature data are then used to create the spectral difference vectors (also called TFI indices) for the detection of TFI signals using the principal component analysis (PCA) method. Since the multichannel correlations of microwave data are often high from natural radiations and low for TFI signatures, the TFI indices are analyzed using the PCA technique, which linearly transforms a set of correlated TFI indices into a much smaller set of uncorrelated principal component (PC) modes, so that radio frequency interference (RFI) signals can be effectively separated from natural radiations. Specifically, the following TFI index vector is defined for TFI detection at the 10.65-GHz horizontal polarization state:

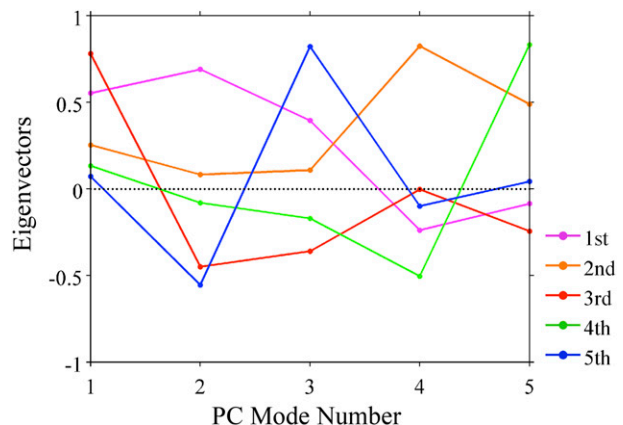


FIG. 3. Five eigenvectors obtained for the same descending swath as in Fig. 2.

$$\mathbf{r}_{10h,i} = \begin{pmatrix} T_{b,10h}^{(n)} - T_{b,18h}^{(n)} \\ T_{b,18h}^{(n)} - T_{b,23h}^{(n)} \\ T_{b,18v}^{(n)} - T_{b,23v}^{(n)} \\ T_{b,23h}^{(n)} - T_{b,36h}^{(n)} \\ T_{b,23v}^{(n)} - T_{b,36v}^{(n)} \end{pmatrix}_i, \quad i = 1, 2, \dots, N. \quad (2a)$$

The vector  $\mathbf{r}_{10h,i}$  consists of the spectral differences of the 10.65-GHz horizontal polarization channels from its neighboring channels (18.7 GHz) at the same polarization state (i.e., the first component in  $\mathbf{r}_{10h,i}$ ), as well as the spectral difference between two neighboring channels with the same polarization states for the remaining frequencies (i.e., the second to the fifth components). Similarly, TFI indices for the 10.65-GHz vertical polarization channel ( $\mathbf{r}_{10v,i}$ ) and the 18.7-GHz horizontal ( $\mathbf{r}_{18h,i}$ ) and vertical ( $\mathbf{r}_{18v,i}$ ) polarization channels are constructed as follows:

$$\mathbf{r}_{10v,i} = \begin{pmatrix} T_{b,10v}^{(n)} - T_{b,18v}^{(n)} \\ T_{b,18h}^{(n)} - T_{b,23h}^{(n)} \\ T_{b,18v}^{(n)} - T_{b,23v}^{(n)} \\ T_{b,23h}^{(n)} - T_{b,36h}^{(n)} \\ T_{b,23v}^{(n)} - T_{b,36v}^{(n)} \end{pmatrix}_i, \quad \mathbf{r}_{18h,i} = \begin{pmatrix} T_{b,18h}^{(n)} - T_{b,23h}^{(n)} \\ T_{b,23h}^{(n)} - T_{b,36h}^{(n)} \\ T_{b,23v}^{(n)} - T_{b,36v}^{(n)} \\ T_{b,36h}^{(n)} - T_{b,89h}^{(n)} \\ T_{b,36v}^{(n)} - T_{b,89v}^{(n)} \end{pmatrix}_i, \quad (2b)$$

$$\mathbf{r}_{18v,i} = \begin{pmatrix} T_{b,18v}^{(n)} - T_{b,23v}^{(n)} \\ T_{b,23h}^{(n)} - T_{b,36h}^{(n)} \\ T_{b,23v}^{(n)} - T_{b,36v}^{(n)} \\ T_{b,36h}^{(n)} - T_{b,89h}^{(n)} \\ T_{b,36v}^{(n)} - T_{b,89v}^{(n)} \end{pmatrix}_i.$$

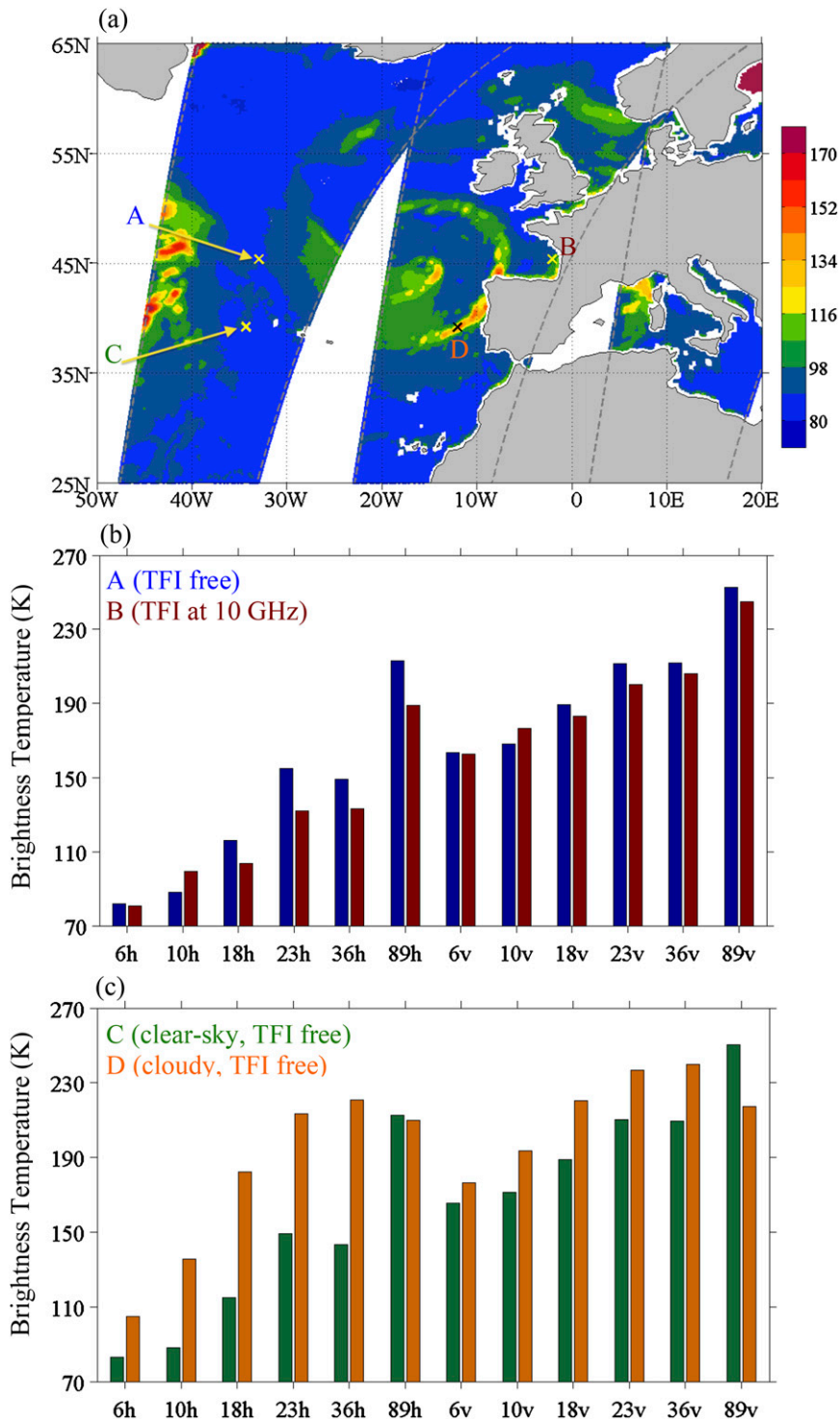


FIG. 4. (a) Spatial distribution of brightness temperatures of the 10.65-GHz horizontally polarized channel on 16 Feb 2011 over ocean around Europe. (b) Brightness temperatures of all AMSR-E channels at four arbitrarily chosen data points A (blue), B (red), C (green), and D (orange) on 16 Feb 2011. Geographic locations of points A–D are indicated in Fig. 4a.

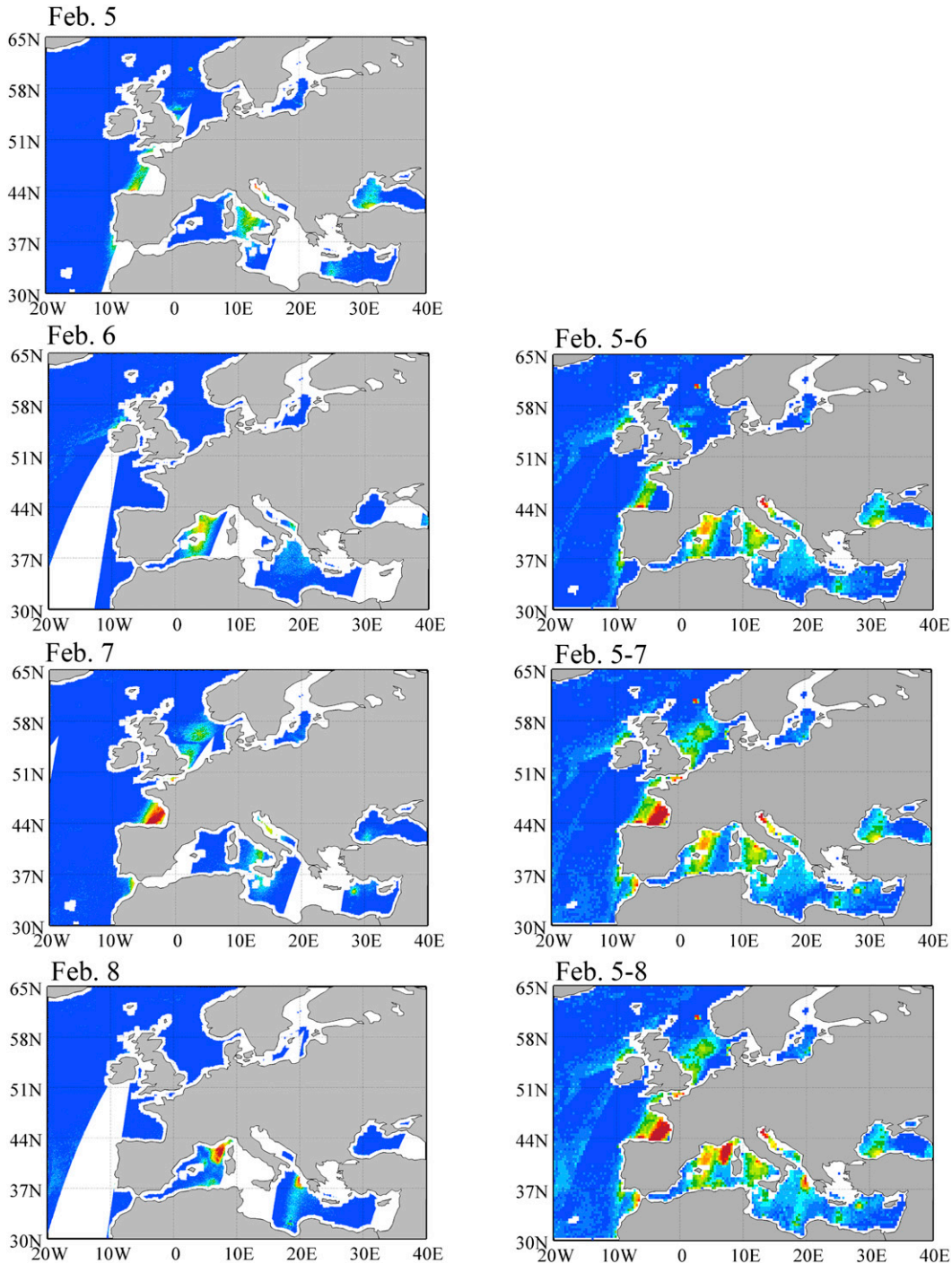


FIG. 5. (left) Daily and (right) accumulative TFI intensity maps at 10.65-GHz horizontal polarization from 5 to 12 Feb 2011 around Europe.

A data matrix  $\mathbf{A}_{5 \times N}$  is constructed from each of the vectors  $\mathbf{r}_{10h,i}$ ,  $\mathbf{r}_{10v,i}$ ,  $\mathbf{r}_{18h,i}$ , and  $\mathbf{r}_{18v,i}$  ( $i = 1, 2, \dots, N$ ). Taking the 10.65-GHz horizontal polarization channel as an example,  $\mathbf{A}_{5 \times N}$  is defined as

$$\mathbf{A}_{5 \times N} = (\mathbf{r}_{10h,1} \quad \mathbf{r}_{10h,2} \quad \dots \quad \mathbf{r}_{10h,N}). \quad (3)$$

Second, a  $5 \times 5$  covariance matrix  $\mathbf{R}_{5 \times 5} = \mathbf{A}\mathbf{A}^T$  is then constructed from  $\mathbf{A}_{5 \times N}$ . The eigenvalues and eigenvectors of the covariance matrix  $\mathbf{R}$  are found by solving the following equation:

$$\mathbf{R}\mathbf{e}_i = \lambda_i \mathbf{e}_i, (i = 1, 2, \dots, 5), \quad (4)$$

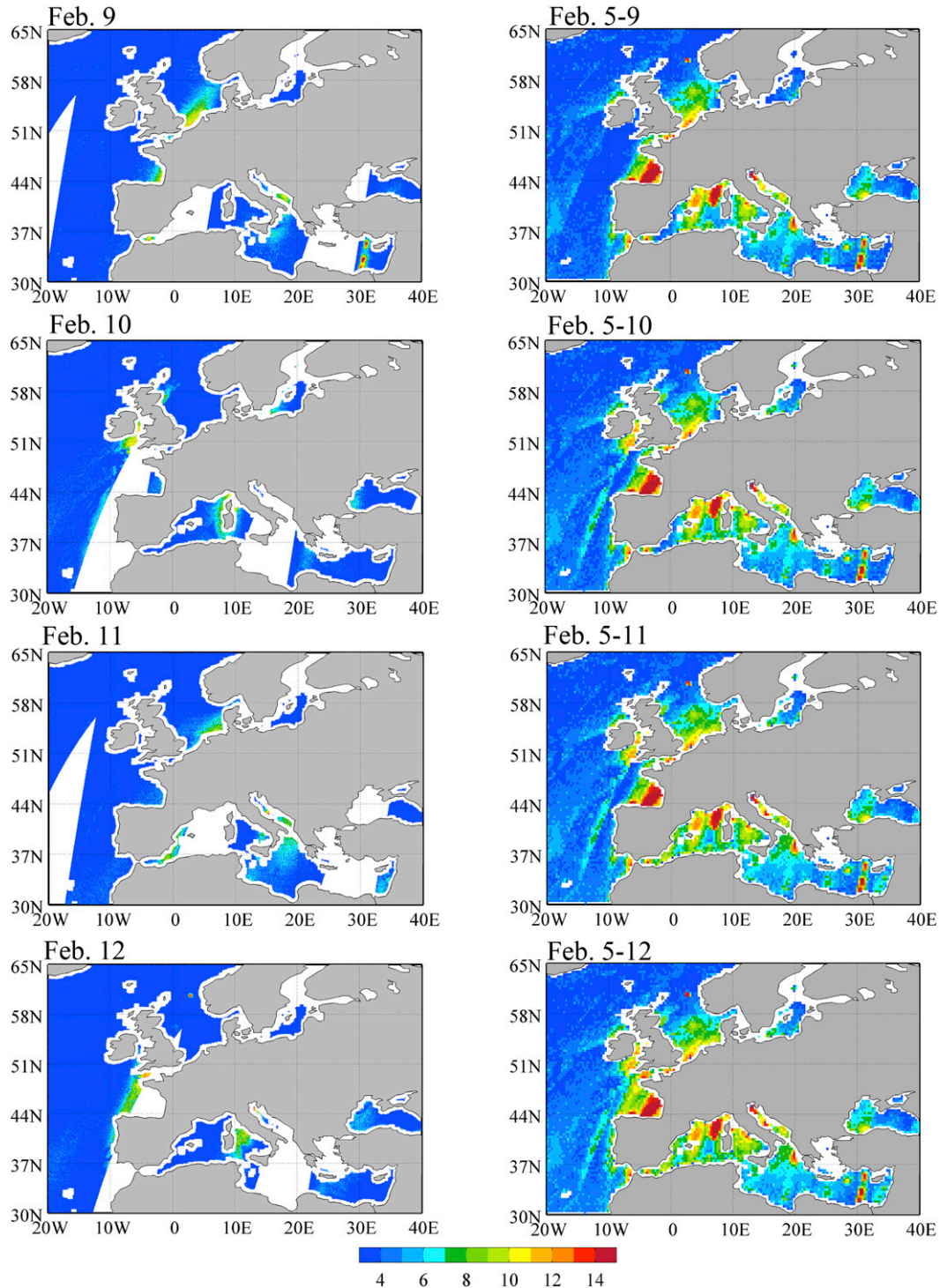


FIG. 5. (Continued)

where  $\lambda_i$  is the  $i$ th eigenvalue and  $\mathbf{e}_i = [e_{1,i}, e_{2,i}, \dots, e_{5,i}]^T$  is called the  $i$ th PC mode,  $i = 1, 2, \dots, 5$ . The  $i$ th eigenvalue  $\lambda_i$  ( $i = 1, 2, \dots, 5$ ) quantifies the variance contribution of the  $i$ th PC mode to the total variance of

data. The eigenvalues/eigenvectors are sorted by the magnitude of the eigenvalue in decreasing order.

Expressing the eigenvalues and eigenvectors in the following matrix form:

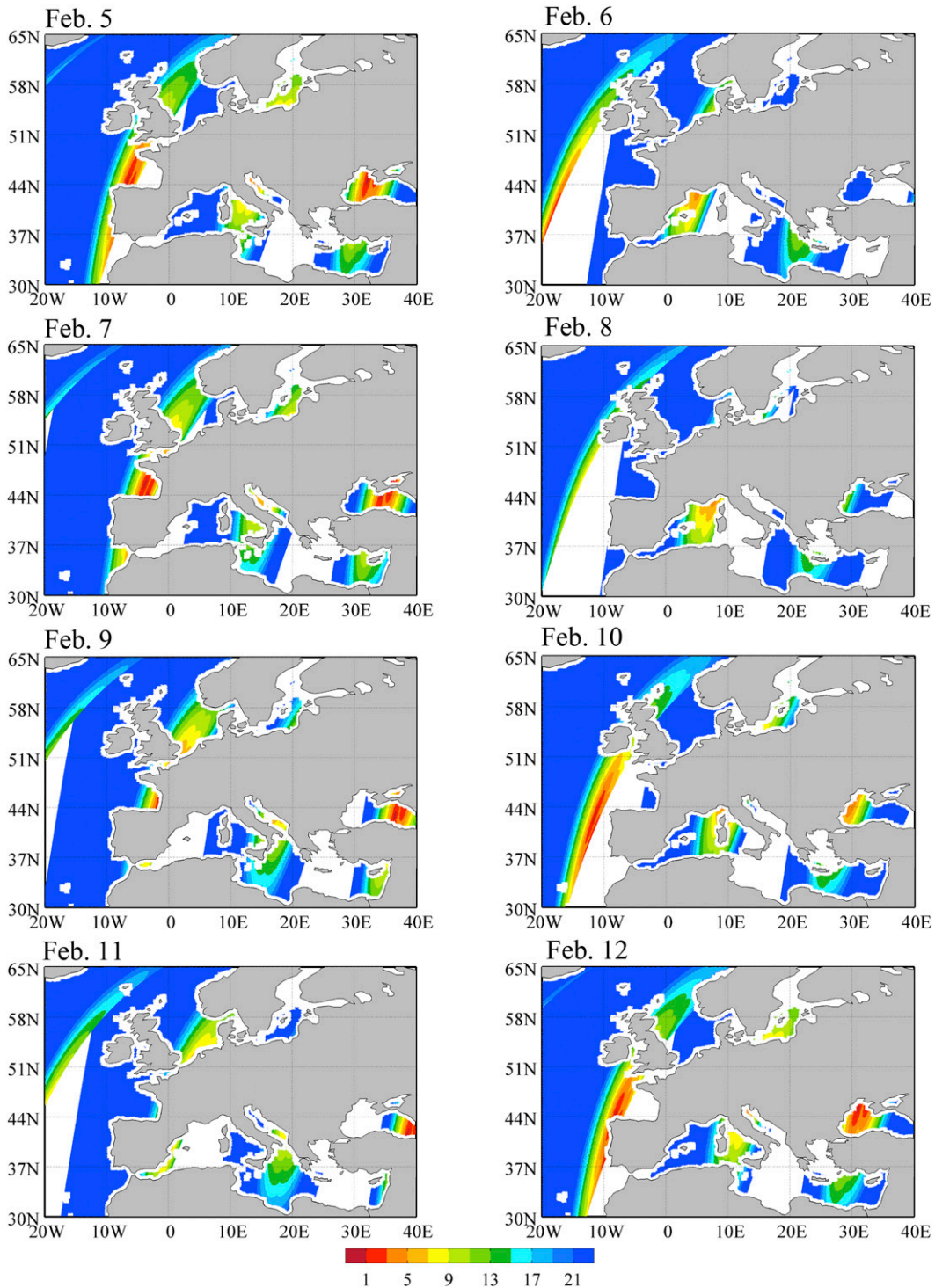


FIG. 6. Satellite glint angle distribution around Europe from the same time period as shown in Fig. 5.

$$\Lambda = \begin{pmatrix} \lambda_1 & \cdots & 0 \\ \vdots & \ddots & \vdots \\ 0 & \cdots & \lambda_5 \end{pmatrix}, \quad \mathbf{E} = [\mathbf{e}_1, \mathbf{e}_2, \dots, \mathbf{e}_5], \quad (5)$$

Eq. (4) can be equivalently written as

$$\mathbf{R}\mathbf{E} = \mathbf{E}\Lambda \quad \text{or} \quad \mathbf{R} = \mathbf{E}\Lambda\mathbf{E}^T. \quad (6)$$

Since  $\mathbf{E}$  is an orthogonal matrix,  $\mathbf{E}^{-1} = \mathbf{E}^T$ .

By projecting the data matrix  $\mathbf{A}$  onto an orthogonal space spanned by the eigenvectors  $\mathbf{e}_1 \ \mathbf{e}_2 \ \dots \ \mathbf{e}_5$ , we obtain the so-called PC coefficients

$$\begin{pmatrix} \mathbf{u}_1 \\ \mathbf{u}_2 \\ \vdots \\ \mathbf{u}_5 \end{pmatrix} = \mathbf{E}^T \mathbf{A}, \quad (7)$$

where  $\mathbf{u}_i = [u_{i,1} \ u_{i,2} \ \dots \ u_{i,N}]$  is the PC coefficient for the  $i$ th PC mode.

The data matrix  $\mathbf{A}$  in Eq. (3) can be reconstructed using PC coefficients and PC modes:

$$\tilde{\mathbf{A}} = \sum_{i=1}^5 \mathbf{e}_i \mathbf{u}_i. \quad (8)$$

The  $i$ th component  $\tilde{\mathbf{A}}_i = \mathbf{e}_i \mathbf{u}_i$  ( $i = 1, 2, \dots, 5$ ) in Eq. (8) represents the data component that accounts for the  $i$ th greatest variance.

Figure 2a shows the spatial distribution of AMSR-E brightness temperature differences between 10.65 and 18.7 GHz at a horizontal polarization state over a portion of a descending swath on 16 February 2011. The corresponding distributions of the five terms in the PC decomposition [Eq. (8)] are provided in Figs. 3b–f. The variances explained by the five vectors are  $3.71 \times 10^5$ ,  $2.78 \times 10^4$ ,  $2.13 \times 10^3$ , 107.6, and  $67.6 \text{ K}^2$ , respectively. It is seen that the first two components,  $\tilde{\mathbf{A}}_1$  and  $\tilde{\mathbf{A}}_2$  (Figs. 2b,c), count for most variances in observations and capture major features of weather systems. The third component ( $\tilde{\mathbf{A}}_3$ ) seems to capture RFI signals near the coastal areas in the Mediterranean Sea, the Bay of Biscay, and the North Sea (Fig. 2d). The fourth and fifth components are more than an order of magnitude smaller than the second and third components. The structures of the five eigenvectors were obtained for the same descending swath as in Fig. 3. It is seen that the third PC mode is characterized by the largest first component and much smaller values for the second to fifth components. Although the first component of the first PC mode is only slightly smaller than that of the third PC mode, the second component of the first PC mode is greater than the first component. This suggests that the first component [e.g.,  $T_{b,10h}^{(n)} - T_{n,18h}^{(n)}$  for TFI detection at 10.65-GHz horizontal polarization] in the TFI index vector dominates the third PC mode. In other words, the TFI signals shall only be present in the first component of the PCA index vector by the definition of the proposed PCA detection algorithm [i.e., Eq. (2)], and are captured by the first row of matrix  $\tilde{\mathbf{A}}_3$ .

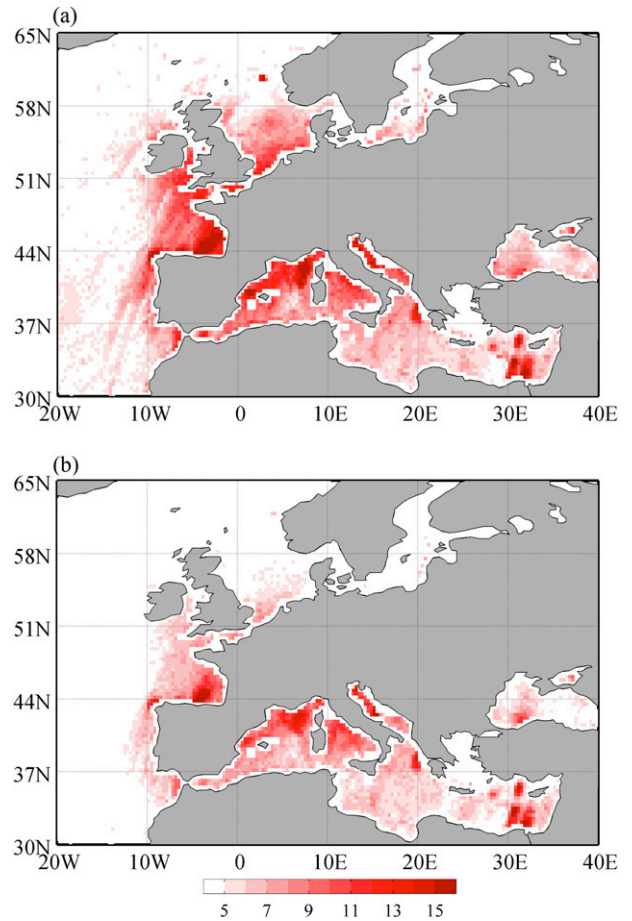


FIG. 7. Monthly accumulated TFI intensity maps for AMSR-E 10.65-GHz channels at (a) horizontal and (b) vertical polarization for all descending portions of AMSR-E orbits from 1 to 18 Feb 2011.

Based on the above-mentioned analysis, the first row of matrix  $\tilde{\mathbf{A}}_3$  is used to represent the TFI intensity vector ( $\mathbf{p}$ ), that is,

$$\tilde{\mathbf{A}}_3 = \mathbf{e}_3 \mathbf{u}_3 = \{(a_3)_{ij}\}, \quad \mathbf{p} = \begin{pmatrix} (a_3)_{11} \sigma_1 \\ (a_3)_{1,2} \sigma_2 \\ \vdots \\ (a_3)_{1,N} \sigma_N \end{pmatrix}, \quad (9)$$

where  $i = 1, 2, \dots, 196$ ,  $j = 1, 2, \dots, N$ , and  $N \approx 2000$  is the number of scan lines in a half orbit of a descending node. The  $i$ th component of the first row of  $\tilde{\mathbf{A}}_3$  is multiplied by the standard deviation of the brightness temperatures at all frequencies at the  $i$ th observation location ( $\sigma_i$ ) to obtain the TFI intensity vector ( $\mathbf{p}$ ). The unit of  $\mathbf{p}$  is thus kelvins.

Since satellite radiances measured at 89.0 GHz are much more sensitive to ice scattering and have a much

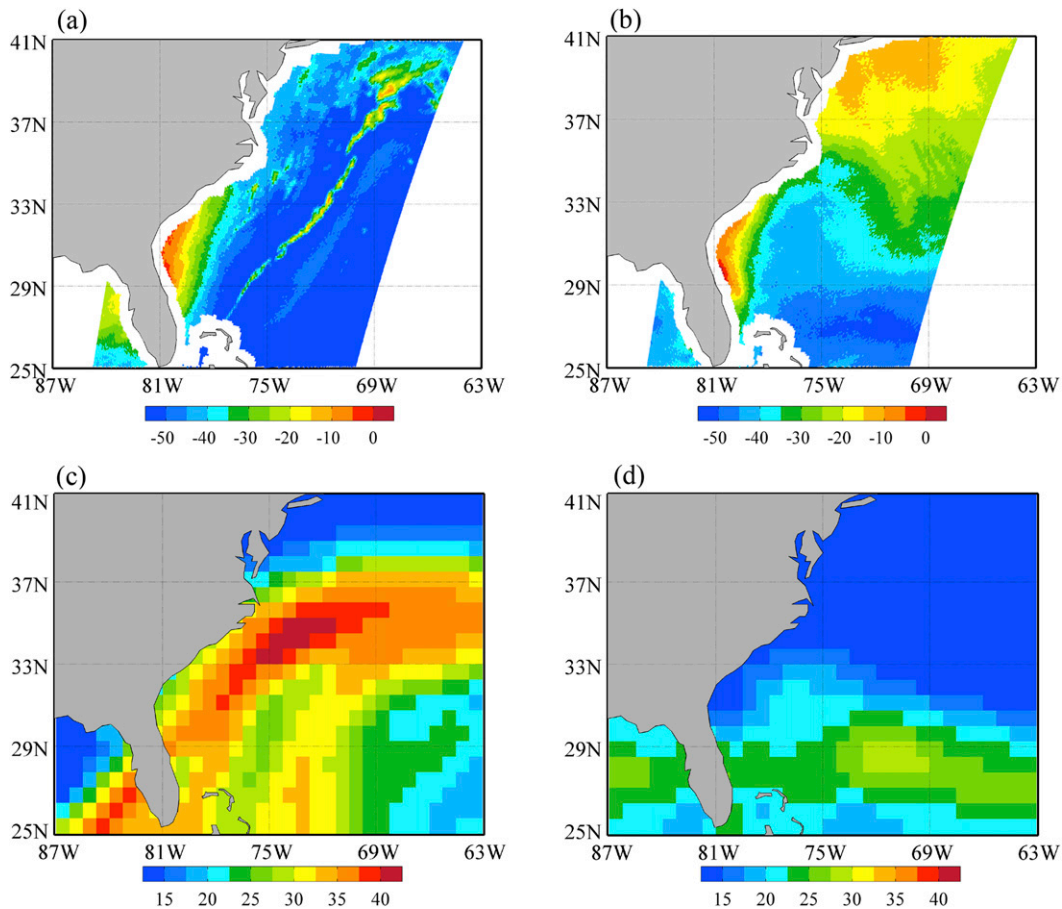


FIG. 8. (a),(b) Spectral differences between  $T_{b,18h}^o$  and  $T_{b,23h}^o$  (K) over a portion of an AMSR-E swath, and (c),(d) total precipitable water ( $\text{kg m}^{-2}$ ) from ERA-Interim data on (left) 8 and (right) 24 Feb 2011.

smaller footprint size than those at lower frequencies, the inclusion of the 89.0-GHz channels in the RFI detection for 18.7 channels causes some noiselike patterns in the TFI intensity results. To remove the “noise,” a two-dimensional five-point smoothing is further applied to the TFI intensity field at both the along-track and across-track directions.

#### 4. Numerical results

##### a. Detection of TFI at 10.65 GHz over ocean

A spatial distribution of horizontally polarized brightness temperatures at 10.65 GHz on 16 February 2011 over the ocean around Europe is provided in Fig. 4a. The measured brightness temperatures at this channel vary from 80 to 170 K. Warmer temperatures are found in cloud and precipitation regions over the Atlantic Ocean as well as near coastal areas in the Mediterranean Sea and the Bay of Biscay. To compare brightness temperatures among various AMSR-E channels in different locations, we select two pairs of data points:

points A and B located at the latitude  $45.4^\circ\text{N}$  and points C and D located at the latitude  $39.2^\circ\text{N}$ . In general, brightness temperatures increase with frequency, and the horizontally polarized brightness temperatures are lower than those at vertical polarization (Figs. 4b,c). However, brightness temperatures at all frequencies at the clear-sky data point A located at  $45.4^\circ\text{N}$ ,  $33.0^\circ\text{W}$  in the middle of the Atlantic ocean are consistently warmer than those at point B except for the 10.65-GHz channels (Fig. 4b), indicating a potential TFI at 10.65 GHz at point B located at  $45.4^\circ\text{N}$ ,  $2.1^\circ\text{W}$ . Brightness temperatures at all the AMSR-E frequencies at the clear-sky data point C located at  $39.2^\circ\text{N}$ ,  $34.3^\circ\text{W}$  in the middle of Atlantic Ocean are consistently colder than those at point D located at  $39.2^\circ\text{N}$ ,  $12.0^\circ\text{W}$  except for the 89-GHz channels (Fig. 4c), indicating the presence of cloud and precipitation at point D. The cloud scattering has the largest impact on the two highest AMSR-E frequency channels at 89.0 GHz. The scattering effects of cloud particles reduce the 89-GHz brightness temperatures at both the vertical and horizontal polarization channels. The impact of cloud on the

remaining AMSR-E channels is mainly due to emission. Since the surface emissivity is lower over ocean, the brightness temperatures in clear-sky conditions are lower than those in cloudy conditions. In other words, the presence of cloud increases the brightness temperatures at the frequencies of 10.65 and 18.7 GHz, which has the same effect as the presence of TFI signals.

Figure 5 presents the daily and accumulative TFI intensity maps at the 10.65-GHz horizontal polarization channel from 5 to 12 February 2011 around western Europe. The exact geographical distribution of the AMSR-E swath over western Europe varies daily. The geographical areas of high TFI intensities shifting with respect to the location within the AMSR-E scan suggest a fixed, directional source. The TFI signals are seen in the Bay of Biscay and the North Sea on the east side of those AMSR-E swaths west of 13.0°E, the Mediterranean Sea, the Adriatic Sea along the longitude 13°E independent of AMSR-E fields of view (FOVs), or on the west side of the AMSR-E swaths east of 13.0°E. The likely sources of these TFI signals are broadcasting signals from European geostationary TV satellites. The European FSS satellites such as *Hot Bird 6, 7A, or 8* operated by Eutelsat1F (<http://www.eutelsat.com/satellites/satellite-fleet.html>) transmit signals within the bands from 10.7 to 12.75 GHz, which are very close to AMSR-E channels at 10.65 GHz. The geostationary satellites identified as *Hot Bird 6, 7A, or 8* were positioned at 13°E longitude to broadcast the X-band signals toward European regions, which are reflected off the ocean surfaces and received together with the earth's passive microwave radiation by AMSR-E. The TFI locations and strength are only found in the descending pass of AMSR-E because the TV satellite signals are in the forward-looking direction of AMSR-E. TFI signals are quite persistent for every AMSR-E overpass with similar observation geometry, eliminating any other possibility, such as mobile sources or weather-system-induced false alarms over the ocean.

As was illustrated in Fig. 1, a key variable reflecting a possible TFI is the angle ( $\alpha$ ) between the satellite viewing vector and the reflected TV signal ray (see Fig. 1). The smaller the  $\alpha$ , the larger the possibility for the reflected TV signals to enter the AMSR-E antenna beams. The closer the glint angle is from the satellite zenith angle, the larger the possibility of RFI. The azimuth angle of the reflected TV signal also impacts how much the reflected TV signals enter the AMSR-E antenna beam. Figure 6 presents a series of spatial distributions of satellite glint angles on those AMSR-E orbital portions presented in Fig. 5. It is seen that TFI signals (left panels in Fig. 5) are found in the areas where satellite glint angles are small (Fig. 6). However, strong TFI signals are not found at the small satellite glint angles when the TV

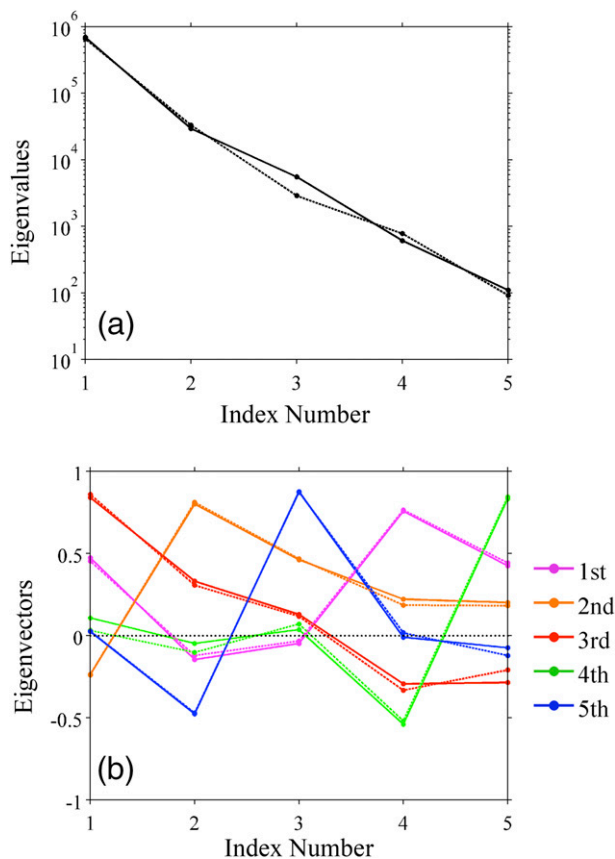


FIG. 9. (a) Eigenvalues and (b) eigenvectors of the data matrices for the TFI detection of 18.7-GHz horizontal polarization of the two swaths in Fig. 8a (solid) and Fig. 8b (dotted).

signal (see Fig. 1) is weak. Thus, the AMSR-E descending overpasses during 5–6 February can cover the coastal regions of the European continent (Fig. 5, top-right panel), since the TFI affected areas on each individual day are much smaller than those of multiple days (the last panel in Fig. 5 for 5–12 February). In other words, there are many RFI-free AMSR-E data over areas (e.g., the Mediterranean Sea, the Bay of Biscay, and the North Sea) where TFI could appear depending on the AMSR-E observation geometry or swath location.

The monthly averaged TFI maps are also derived within the  $0.2^\circ \times 0.2^\circ$  grid resolution for the AMSR-E 10.65-GHz channels from 1 to 18 February 2011 and are shown in Fig. 7. With the PCA-based method, the false alarms of the TFI signals are not found over the global ocean, since the weather systems associated with high surface wind, clouds, and precipitation are clearly separated from the TFI signals.

#### b. Detection of TFI at 18.7 GHz over ocean

There are three DirecTV satellites—DirecTV-10, DirecTV-11, and DirecTV-12—that transmit the signals

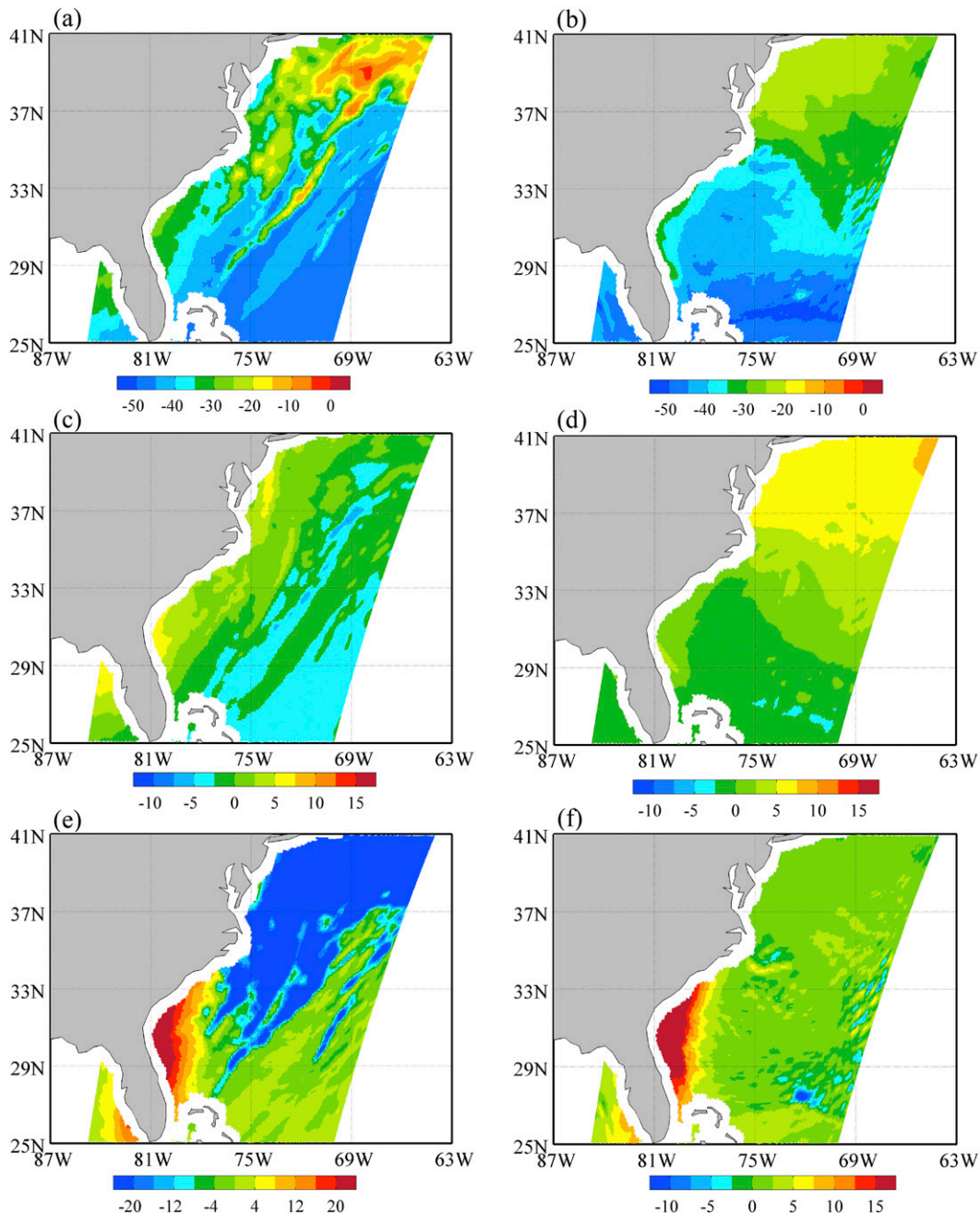


FIG. 10. Spatial distributions of the first component (e.g.,  $T_{b,18h}^o - T_{b,23h}^o$ ) in the data decomposition matrices (a),(b)  $\mathbf{A}_1$ , (c),(d)  $\mathbf{A}_2$ , and (e),(f)  $\mathbf{A}_3$  over a portion of an AMSR-E swath on (left) 8 and (right) 24 Feb 2011.

to the United States at the K band near the AMSR-E 18.7-GHz channels (Wiltshire et al. 2004; Wentz and Meissner 2000). DirecTV-10 and DirecTV-12 are positioned at 103°W and DirecTV-11 at 99°W above the equator. All three satellites use a nationwide beam for general broadcasting and multiple spot beams for local high-definition channels. The nationwide beam for general broadcasting operates from 18.3 to 18.6 GHz, and the

multiple spot beams for local high-definition channels operate from 18.6 to 18.8 GHz. Therefore, the AMSR-E channels at 18.7 GHz could be interfered with the DirecTV signals reflected off the ocean surfaces around the coastal areas of the United States.

Two cases are used to show how the proposed PCA method works for the RFI detection over oceans for the 18.7-GHz channels. The spectral differences between

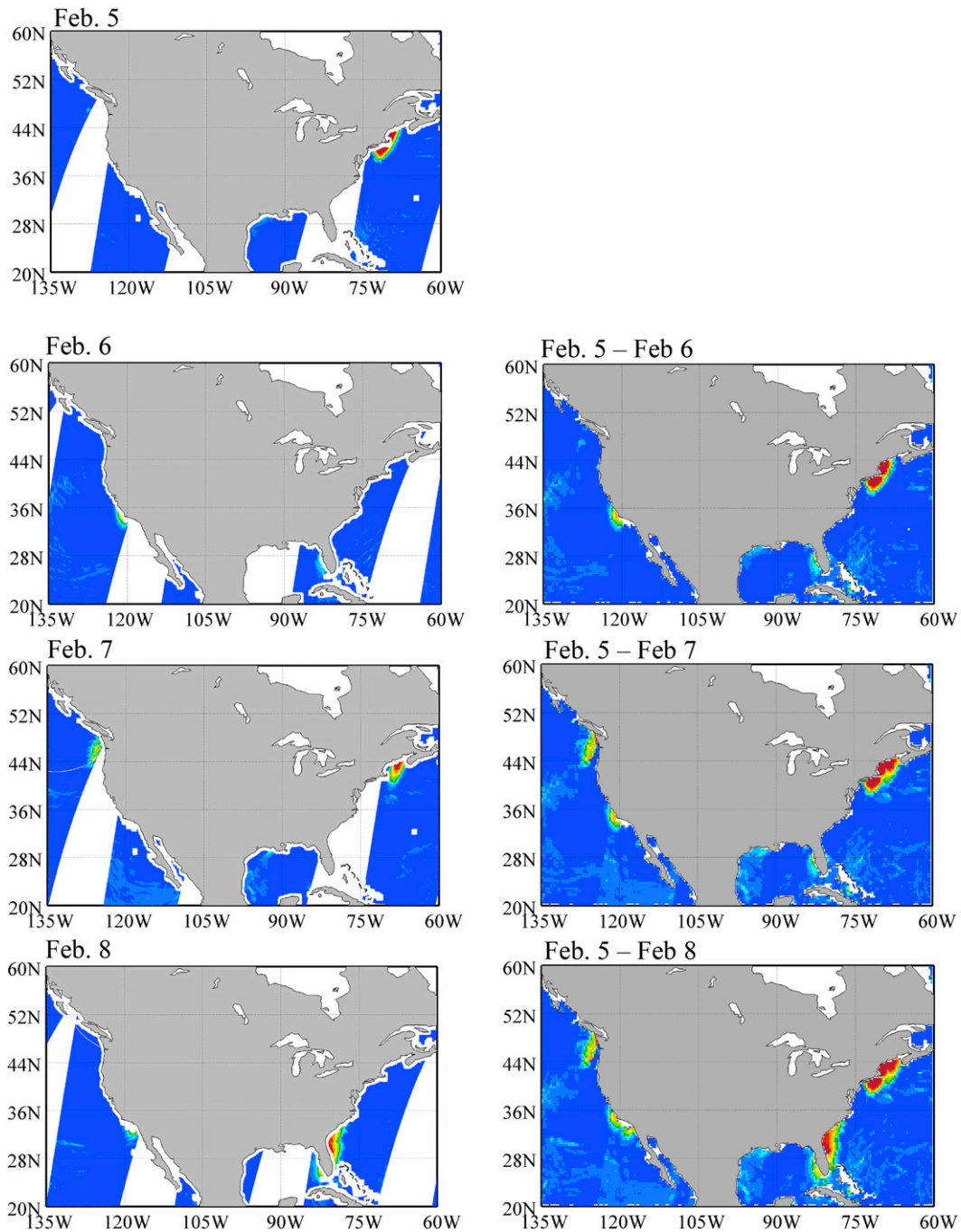


FIG. 11. (left) Daily and (right) accumulative TFI intensity maps at 18.7-GHz horizontal polarization from 5 to 12 Feb 2011 around the United States.

the 18.7- and 23-GHz channels (i.e.,  $T_{b,18h}^o - T_{b,23h}^o$ ) over two AMSR-E swaths near the East Coast of the United States are presented in Fig. 8. The case on 8 February 2011 involved a cloud system, whereas the case on 24 February represented a more fair-weather condition. The total precipitable water distributions on both days

from the Interim European Centre for Medium-Range Weather Forecasts Re-Analysis (ERA-Interim) data are provided as a reference. Positive spectral differences near the coast of Florida are found on both days (Figs. 8a,b), within a cloudy system away from the East Coast on 8 February (Fig. 8a) and a relatively drier region near the

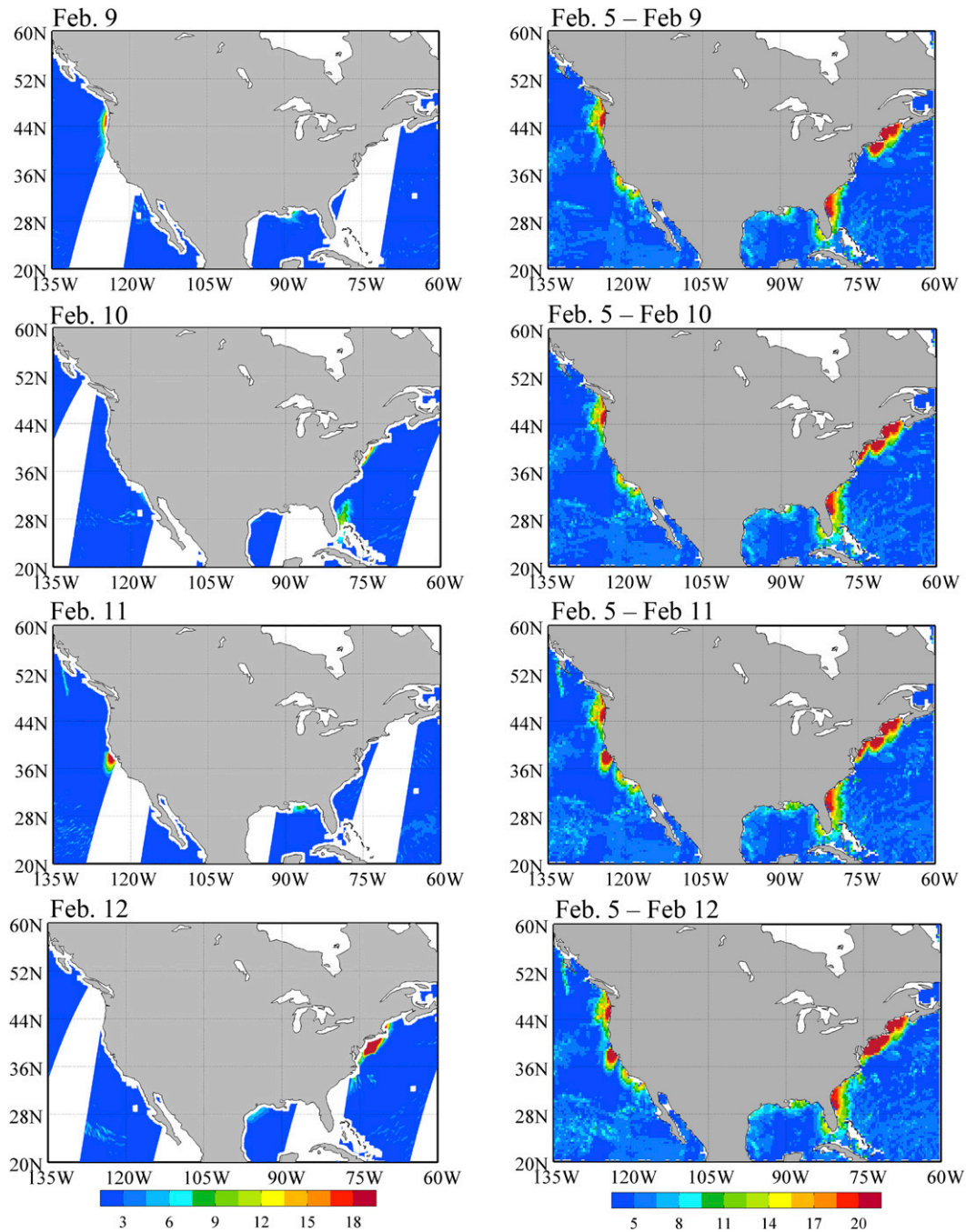


FIG. 11. (Continued)

coastal area in the middle latitudes on 24 February 2011 (Fig. 8b). It seems that the spectral difference alone cannot indicate TFI in the AMSR-E observations at the 18.7-GHz horizontal polarization channel.

Figure 9 presents the eigenvalues (Fig. 9a) and eigenvectors (Fig. 9b) for the TFI detection of 18.7-GHz horizontal polarization of the data matrices of the two

swaths in Fig. 8. The variances explained by the five eigenvectors decrease exponentially. The third eigenvector has the largest first component and decreases monotonically with the index number. The largest values for the first, second, fourth, and fifth components are in the fourth, second, fifth, and third components, respectively. The first three PCA components of the data matrix

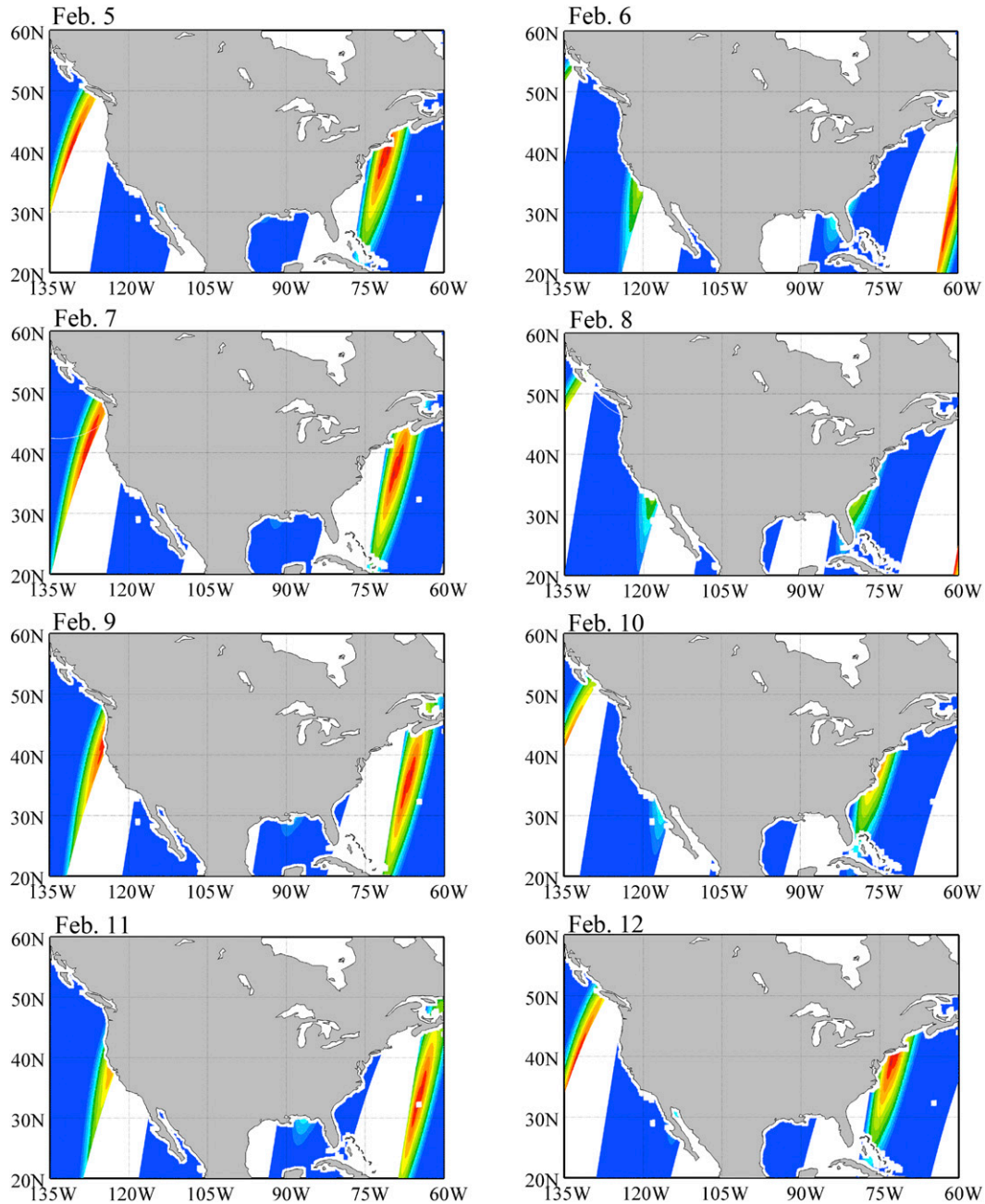


FIG. 12. Satellite glint angle distribution around North America from the same time period as that shown in Fig. 11.

corresponding to the TFI index vectors for the 18.7-GHz horizontal polarization channel ( $\mathbf{R}_{18h,i}$ ) are shown in Fig. 10 over the same portions of the two AMSR-E swaths near the East Coast of the United States in Fig. 8. The fourth and the fifth PCA components are very small (figures omitted). It is seen that the weather-related signals are mostly described by the first two PCA components (Figs. 10a–d). The third PCA component

(Figs. 10e,f) captures strong TFI signals near the east coast of Florida and some weak TFI signals near the west coast of Miami.

Figure 11 shows a series of daily and accumulated TFI intensity maps at 18.7-GHz horizontal polarization from 5 to 12 February 2011 around the United States using the proposed third PCA component method. The TFI-contaminated AMSR-E data are found near the

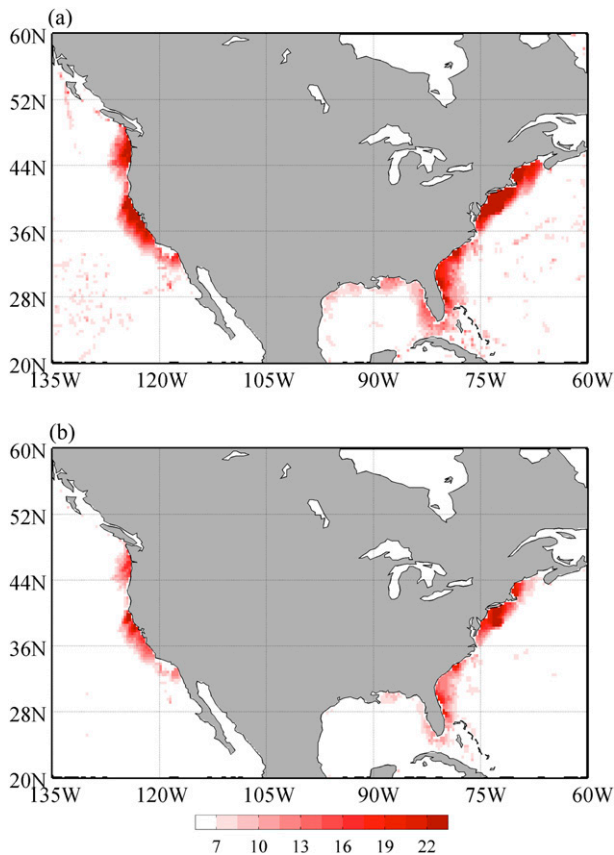


FIG. 13. Monthly accumulated TFI intensity maps for AMSR-E 18.7-GHz channels at (a) horizontal and (b) vertical polarization for all descending portions of AMSR-E orbits from 1 to 18 Feb 2011.

eastern edge of the AMSR-E swath west of  $99^\circ$  or  $103^\circ\text{W}$ , and on the west side of the AMSR-E swath east of  $99^\circ$  or  $103^\circ\text{W}$  around the coastal areas. Such a characteristic of TFI contamination of AMSR-E data is

determined by the geometric relationship between the *Aqua* and the DirecTV satellites. Therefore, there are many TFI-free AMSR-E data over the coastal areas, depending on their scan positions.

The spatial distributions of satellite glint angles on those AMSR-E orbital portions presented in Fig. 11 are shown in Fig. 12. Again, TFI signals (left panels in Fig. 11) are found in the areas where the satellite glint angles are small (Fig. 11). Again, a 2-day coverage of AMSR-E descending overpasses during 5 and 6 February show the smallest TFI signals (Fig. 11, top-right panel), and there are many TFI-free AMSR-E data near the east and west coastal areas of the United States. The TFI-contaminated data are very limited, depending on AMSR-E swath geometry.

By examining the monthly averaged global TFI intensity maps for AMSR-E 18.7-GHz channels for all descending portions of AMSR-E orbits from 1 to 18 February 2011, we found that TFI signals are located on the East and West Coasts of the United States and on the Gulf Coast (see Fig. 13). It is therefore important to separate the weather signals from TFI-contaminated signals in these coastal regions, so that the clear AMSR-E data can be used for the geophysical parameter retrieval and data assimilation.

### c. Applications of the new algorithm for TFI detection over global ocean

In sections 4a and 4b, the TFI detection algorithm was applied to a single swath. It is important to check if the third eigenvector for the oceanic TFI detection at a specified frequency (10.65 or 18.7 GHz) has the same structure as mentioned above for all swaths globally. Figure 14 shows the third eigenvector of 10.65-GHz horizontal polarization for all descending swaths on 16 February 2011, as well as the third eigenvector of

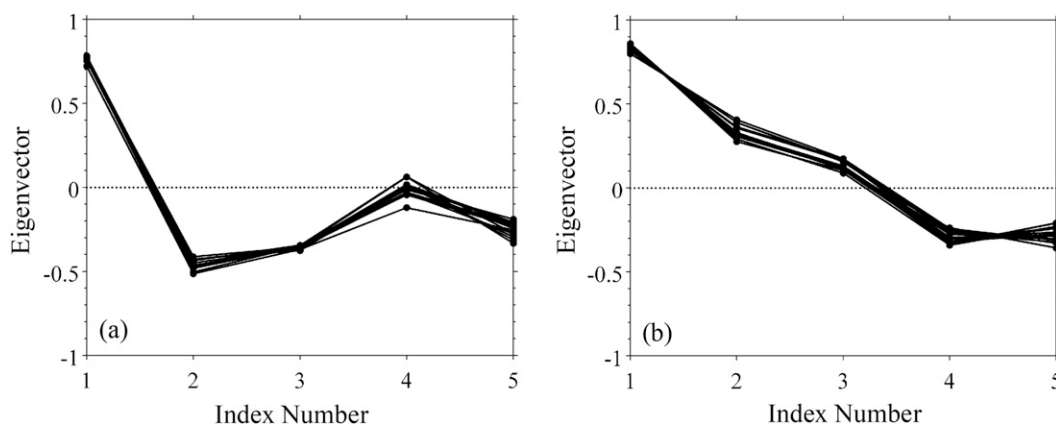


FIG. 14. (a) Third eigenvectors of the 10.65-GHz horizontal polarization channel for all descending swaths on 16 Feb 2011. (b) Third eigenvectors of the 18.7-GHz horizontal polarization channel for all descending swaths on 24 Feb 2011.

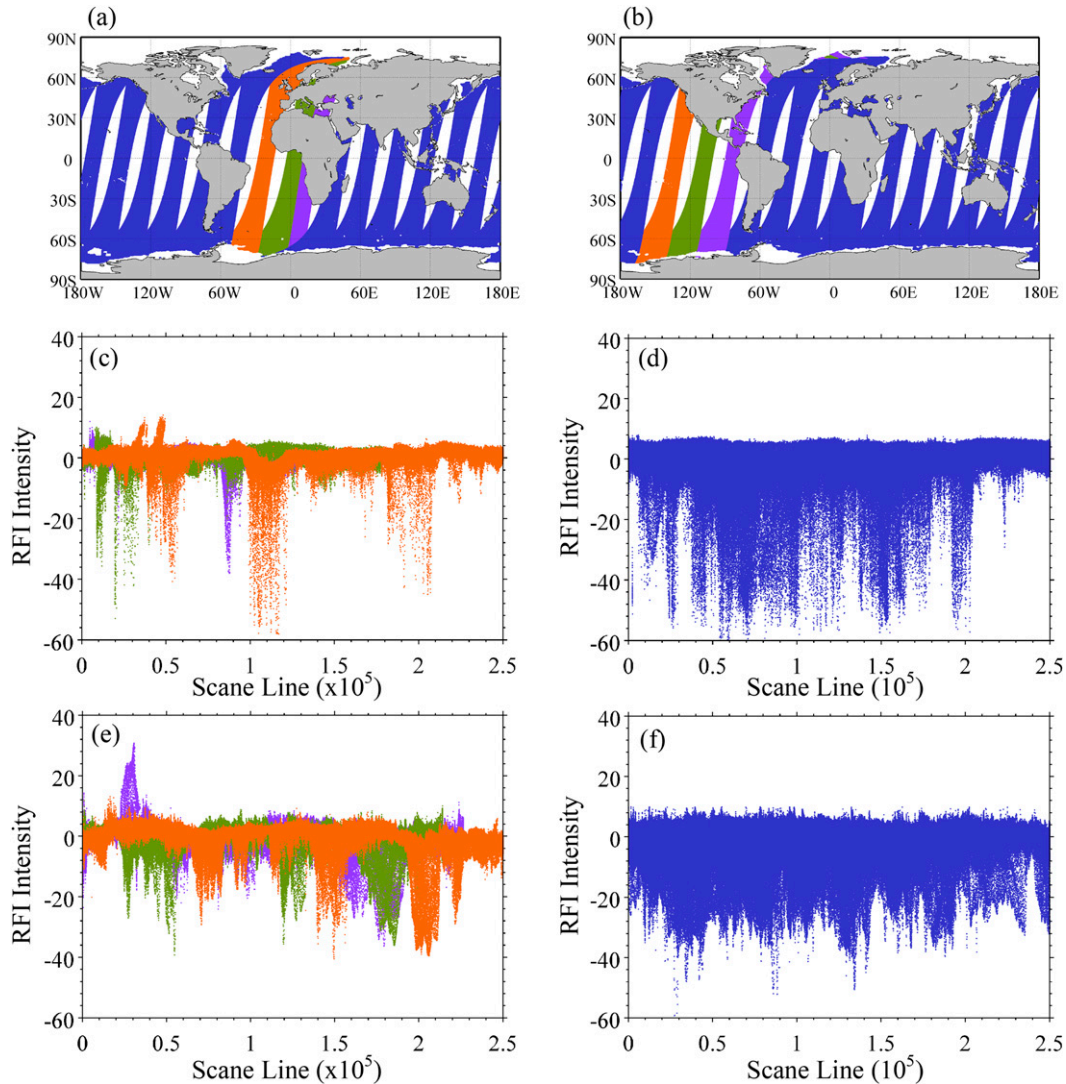


FIG. 15. Global distributions of all AMSR-E descending swaths on (a) 16 and (b) 24 Feb 2011. (c),(d) TFI intensities at the 10.65-GHz horizontal polarization state of the three swaths with (left) TFI signals (orange, green, and purple) and (right) all other swaths (blue) on 16 Feb. (e),(f) As in (c),(d), but for 18.7 GHz on 24 Feb 2011.

the 18.7-GHz horizontal polarization channel for all descending swaths on 24 February 2011. The structure of the third eigenvector for the oceanic TFI detection at a specified frequency (10.65 or 18.7 GHz) is nearly the same for all swaths globally. Both are characterized by the largest value of the first component. The global distributions of all AMSR-E descending swaths on 16 and 24 February 2011 are presented in Figs. 15a,b. On both days, there are three swaths over which TFI signals are detected, which are indicated in orange, green, and purple. TFI intensities over all swaths are provided in Figs. 15c–f. The TFI intensity is bounded below a value within 5–10 K (e.g., an upper limit) for all the AMSR-E TFI-free swaths (Figs. 15d,f). However, for the three

swaths with TFI signals detected, the TFI intensity exceeds the above-mentioned upper limit.

## 5. Summary and conclusions

TFI detection over ocean for satellite low-frequency microwave imager radiances is important and challenging. TFI must be reliably identified before the microwave imager data are used for either geophysical retrievals or NWP data assimilation. In this paper, a PCA-based method is proposed and tested for detecting TFI signals in AMSR-E data over ocean.

The new PCA-based method takes into account the multichannel correlations for natural ocean surface

radiations, as well as the decorrelation between different frequencies in the presence of TFI signals. A strong TFI is visible for X- and K-band channels at both horizontal and vertical polarization over ocean near coastal regions over Europe and the United States, respectively. Consistent with the cause of the ocean TFI signals, measurements of the natural thermal emission from the AMSR-E satellite over ocean are interfered with by the geostationary satellite television (TV) signals reflected off the ocean surfaces. Strong TFI signals are populated along the eastern, southern, and western coastal areas of the United States in the AMSR-E K-band data in descending node. Strong oceanic TFI signals are found in the AMSR-E X-band data in the Mediterranean Sea, the Adriatic Sea north of Italy, and around Sicily. The TFI locations are also quite persistent for every AMSR-E descending swath passing over these regions with similar observation geometry. The likely sources of the oceanic TFI occurrences are the broadcasting signals from European geostationary television (TV) satellites above the equator.

The proposed PCA-based oceanic TFI detection algorithm works at any geographical location over the global ocean, regions with or without the presence of cloud and high water vapor weather systems. Being applicable at the granule data level, it offers a global oceanic TFI detection method for AMSR-E data at X and K bands.

*Acknowledgments.* This work was jointly supported by Chinese Ministry of Science and Technology Project 2010CB951600 and NOAA JPSS GCOM-W project. The authors thank NASA and the National Space Development Agency of Japan (JAXA) for providing *Aqua* AMSR-E data to operational centers as well as to the research community.

#### REFERENCES

- Adams, I. S., M. H. Bettenhausen, P. W. Gaiser, and W. Johnston, 2010: Identification of ocean-reflected radio frequency interference using WindSat retrieval chi-square probability. *IEEE Geosci. Remote Sens. Lett.*, **7**, 406–410, doi:10.1109/LGRS.2009.2037446.
- Kawanishi, T., and Coauthors, 2003: The Advanced Microwave Scanning Radiometer for the Earth Observing System (AMSR-E), NASA's contribution to the EOS for global energy and water cycle studies. *IEEE Trans. Geosci. Remote Sens.*, **41**, 184–194, doi:10.1109/TGRS.2002.808331.
- Kelly, R. E., A. T. Chang, L. Tsang, and J. L. Foster, 2003: A prototype AMSR-E global snow area and snow depth algorithm. *IEEE Trans. Geosci. Remote Sens.*, **41**, 230–242, doi:10.1109/TGRS.2003.809118.
- Li, L., P. W. Gaiser, M. Bettenhausen, and W. Johnston, 2006: WindSat radio-frequency interference signature and its identification over land and ocean. *IEEE Trans. Geosci. Remote Sens.*, **44**, 530–539, doi:10.1109/TGRS.2005.862503.
- Njoku, E. G., and L. Li, 1999: Retrieval of land surface parameters using passive microwave measurements at 6–18 GHz. *IEEE Trans. Geosci. Remote Sens.*, **37**, 79–93, doi:10.1109/36.739125.
- , T. J. Jackson, V. Lakshmi, T. K. Chan, and S. V. Nghiem, 2003: Soil moisture retrieval from AMSR-E. *IEEE Trans. Geosci. Remote Sens.*, **41**, 215–229, doi:10.1109/TGRS.2002.808243.
- Truesdale, D., 2013: A probability distribution method for detecting radio-frequency interference in WindSat observations. *IEEE Trans. Geosci. Remote Sens.*, **51**, 3780–3788, doi:10.1109/TGRS.2012.2223473.
- Wentz, F. J., and T. Meissner, 2000: Algorithm theoretical basis document (ATBD), version 2: AMSR ocean algorithm. RSS Tech. Proposal 121599A-1, 66 pp. [Available online at [http://images.remss.com/papers/amr/AMSR\\_Ocean\\_Algorithm\\_Version\\_2.pdf](http://images.remss.com/papers/amr/AMSR_Ocean_Algorithm_Version_2.pdf).]
- Wilheit, T., C. D. Kummerow, and R. Ferraro, 2003: NASDA rainfall algorithms for AMSR-E. *IEEE Trans. Geosci. Remote Sens.*, **41**, 204–214, doi:10.1109/TGRS.2002.808312.
- Wiltshire, W. M., M. D. Nilsson, and F. B. Campbell, 2004: Application for authorization to launch and operate DirecTV 10, a partial replacement Ka-band satellite, at 103 deg. WL. FCC Form 312, Exhibit 43, Harris, Wiltshire and Grannis LLP Doc., 86 pp. [Available online at [http://licensing.fcc.gov/myibfs/download.do?attachment\\_key=421286](http://licensing.fcc.gov/myibfs/download.do?attachment_key=421286).]
- Zhao, J., X. Zou, and F. Weng, 2013: WindSat radio-frequency interference signature and its identification over Greenland and Antarctic. *IEEE Trans. Geosci. Remote Sens.*, **51**, 4830–4839, doi:10.1109/TGRS.2012.2230634.
- Zou, X., J. Zhao, F. Weng, and Z. Qin, 2012: Detection of radio-frequency interference signal over land from FY-3B Microwave Radiation Imager (MWRI). *IEEE Trans. Geosci. Remote Sens.*, **50**, 4994–5003, doi:10.1109/TGRS.2012.2191792.